Geophysical Journal International

Geophys. J. Int. (2016) **205,** 988–994
Advance Access publication 2016 February 15
GJI Seismology

doi: 10.1093/gji/ggw065

Complex rupture of the *M*6.3 2015 March 10 Bucaramanga earthquake: evidence of strong weakening process

P. Poli,[1] G.A. Prieto,[1] C.Q. Yu,[1] M. Florez,[1] H. Agurto-Detzel,[2] T.D. Mikesell,[1,3] G. Chen,[1] V. Dionicio[4] and P. Pedraza[4]

[1]*Earth, Atmospheric and Planetary Sciences, Massachusetts Institute of Technology, Cambridge, MA, USA. E-mail: ppoli@mit.edu*
[2]*Instituto de Astronomia, Geofísica e Ciências Atmosféricas, Universidade de São Paulo, Brazil*
[3]*Center for Geophysical Investigation of the Shallow Subsurface, Department of Geosciences, Boise State University, Boise, ID, USA*
[4]*Servicio Geológico Colombiano, Bogotá, Colombia*

Accepted 2016 February 11. Received 2016 February 2; in original form 2015 August 25

SUMMARY

We use seismic waves for a magnitude 6.3 intermediate-depth (160 km) earthquake in the Bucaramanga Nest, Colombia, to infer a complex rupture process with two distinct stages, characterized by different rupture velocities possibly controlled by the evolution of strength on the fault. Our integrated data processing permitted to precisely characterize the multistage rupture and the presence of a strong weakening event. The resulting seismic radiation is interpreted as resulting from an extreme weakening due to a cascading thermal shear runaway, with an initial inefficient radiation process followed by a fast and dynamic efficient rupture. Our results imply dynamic complexity of the seismic rupture deep inside the Earth, and may help to give some new insights about the physical mechanism of intermediate-depth earthquakes.

Key words: Earthquake dynamics; Earthquake source observations; Body waves.

INTRODUCTION

The physical process responsible for intermediate-depth and deep focus earthquakes is still poorly understood and remains one of the outstanding questions in geophysics (Green 1995; Frohlich 2006; Houston 2007). The high temperatures and pressures hundreds of kilometres deep inside the Earth should inhibit the occurrence of brittle failure, however global seismic networks routinely locate earthquakes at depths larger than 50 km.

Shallow (0–50 km), intermediate-depth (50–350 km), and deep (350+ km) earthquakes all represent shear slip on a fault; however, anomalous behaviour has been reported for deeper events including: significant non-double couple focal mechanisms (Richardson & Jordan 2002), radiated seismic energies (Wiens 2001), *b*-values and aftershock sequences (Wiens & Gilbert 1996; Frohlich 2006; Houston 2007) and source durations and stress drops (Frohlich 2006; Houston 2007; Poli & Prieto 2014) that often differ from values observed for shallow events. Detailed comparison between deep earthquakes shows a large diversity of rupture behaviour (Wiens 2001), with mainly slow rupture velocity and low efficiency events observed in warm subduction slabs, and faster more energetic ruptures in cold slabs (Kanamori *et al*. 1998; Chen *et al.* 2014; Zhan *et al.* 2014a). Unfortunately, our ability to resolve the fundamental rupture parameters (e.g. geometry and rupture velocity) remains inadequate due to the limited resolution offered by observations at teleseismic distances (Zhan *et al.* 2014a).

A magnitude (M_w) 6.3 earthquake on 2015 March 10 occurred at ∼160 km depth in the Bucaramanga Nest (BN) in northern South America (Fig. 1). The BN is the densest concentration of intermediate-depth earthquakes in the world (Prieto *et al.* 2012). In this contribution we the study the rupture process for the *M*6.3 Bucaramanga event, showing a complex rupture process with evidence for a strong weakening event during the dynamic rupture.

Focal mechanism

We invert broad-band seismic records at regional distances (100–500 km) to retrieve the moment tensor and centroid time/position. For the regional inversion we use the ISOLA software (Sokos & Zahradnik 2008) and obtain a similar moment tensor solution to that obtained teleseismically from the gCMT, NEIC and FDSN (Table 1). For calculating the Green's functions we use the 1-D velocity model from the Colombian Geological Survey, which is based on the results by (Ojeda & Haskov 2001).

Results were obtained in the frequency band 0.04–0.1 Hz (see Fig. S1). Higher frequencies gave a poorer fitting due to the simplicity of the used velocity model and relatively large hypocentral distances. Nevertheless, a common feature found in all tested combinations of stations, frequency bands (up to 0.3 Hz) and source positions, is the stability of the obtained focal mechanism, always showing normal faulting similar to the final solution. Our results (Figs 1, S1 and S2) show a dominant double-couple solution with a 7–10 per cent CLVD component consistent with the dominant stress field around the BN (Cortés & Angelier 2005; Prieto *et al.* 2012), and similar to other reported MT solutions (Table 1). Regional and

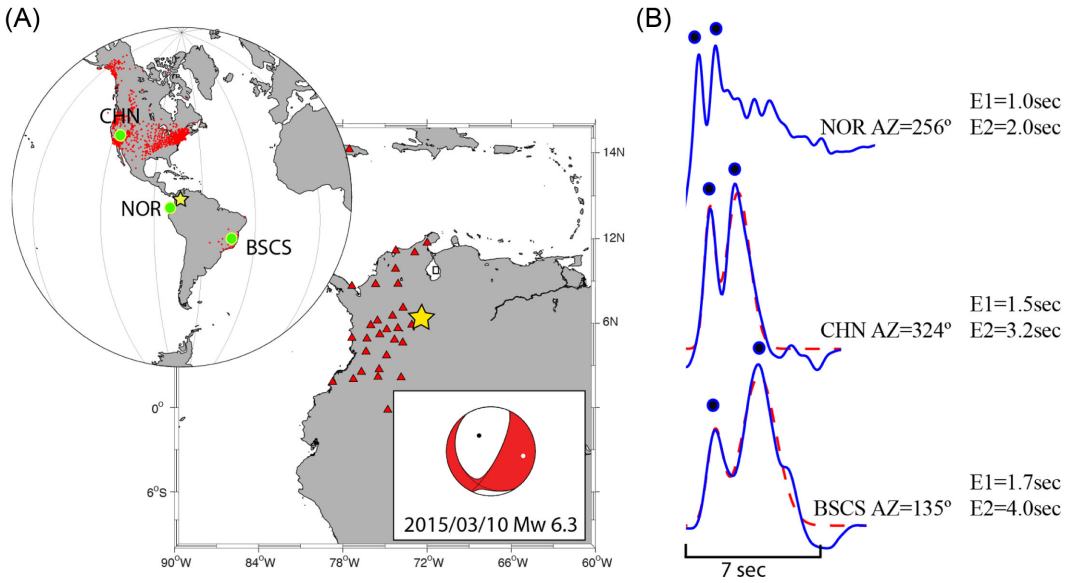

Figure 1. Map showing the position of the M_w 6.3 Bucaramanga Nest (star) earthquake and the seismic station used in this study (red triangles and dots). (a) Focal mechanism obtained by inversion of regional data at red triangles. The red dots on the global map are the global stations included in our study. (b) Apparent (blue) and predicted (red) STFs at selected stations (green dots in a) showing a clear rupture directivity effect on the *P*-wave pulses. Blue dots indicate the arrival times of the centroid for E1 and E2. Name of the station, azimuth and centroid time (w.r.t. origin time) are reported.

Table 1. Moment tensor (MT) using regional data (this study) and reported by NEIC and the Global CMT. Per cent DC shows the percentage of pure double-couple mechanism, with the rest mostly associated with CLVD. FDSN report does not include per cent DC (Vallee *et al.* 2011).

Source	$M_0 \times 10^{18}$ (N.m)	M_w	Strike/dip/rake 1	Strike/dip/rake 2	Per cent DC	Method
This study	3.245	6.27	26/76/−67	147/26/−147	93	Regional MT
NEIC	2.671	6.22	28/77/−73	154/21/−142	95	Teleseismic body wave
GCMT	3.016	6.25	26/76/−66	144/27/−149	93	Teleseismic centroid MT
FDSN	3.040	6.25	28/78/−64	141/29/−153	N.A.	Teleseismic scardec

teleseismic *P*- and SH-polarities provide further constraints on the MT (Figs S3 and S4).

Waveform analysis and details of the rupture process

A closer look of seismic waveforms, recorded at both regional and teleseismic distances, indicates a more complicated rupture process. Instead of a single energy burst, the M_w 6.3 event can be divided into two major subevents E1 and E2 (Figs 1, S3 and S4). Systematic delay between the times of E1 and E2 as well as the broadening of the seismic waveforms as a function of azimuth shows a directivity effect, related to directional rupture process on a finite fault.

To determine the rupture history and constrain the physical process associated with this M_w 6.3 intermediate-depth earthquake, we analysed seismic data from both regional (<10°) and teleseismic (30–90°) distances. Because of the moderate size of the event, the first step in studying the directivity is to improve the signal-to-noise ratio of the teleseismic *P* waves. To that end, we constructed several subarrays composed of stations from the global network (GNS), USArray (TA) and the Brazilian network (RSBR; Bianchi *et al.* 2014). Other available data in Europe or Chile are in the nodal plane of the Focal mechanism and have little energy in the *P* arrival. Fig. S4 shows a selection of apparent source time functions at teleseismic distances, where two clear subevents are visible. The STFs (source time function) are obtained using similar processing to that used for receiver function analysis (e.g. Rondenay *et al.* 2005). First, the waveforms filtered between 0.01 and 2 Hz, for arrays of closely spaced sensors are aligned using a multichannel cross correlation (MCCC) around the *P*-wave arrival (VanDecar & Crosson 1990). Once aligned, the source signature is extracted using Principal Component Analysis (PCA; Yu *et al.* 2013), which preserves the amplitudes. For each teleseismic subarray we obtain a STF as plotted in Fig. S4. We estimate regional STFs using a small subset of BN earthquakes (M_w 4–5) and applying empirical Green's function deconvolution (e.g. Prieto *et al.* 2009) to the main shock waveforms.

To quantitatively estimate the time and geometric characteristic of the sub events, we use an inversion algorithm similar to Zhan *et al.* (2014b), fitting the STFs with one Gaussian for each subevent. In our inversion we only fixed the number of subevents and the fitting is done using a non-linear algorithm (Seber & Wild 2003), which provides as output amplitude, polarity, standard deviation (duration) and the centroid time for each Gaussian (Figs 1, 3 and S3).

We then estimate the relative locations of the hypocentre, E1 and E2 centroids, using a double-difference location algorithm (Waldhauser & Ellsworth 2000; Fig. 2). The combination of teleseismic and regional data allows for well-constrained centroid locations (Fig. S6), in particular the regional data allows for constraining the vertical separation. The centroid of E1 is located ~3.7 km from the hypocentre and is 1.5 km deeper, while that of E2 is ~6.7 km from the hypocentre and is 7 km shallower. All location and source parameters for E1 and E2 are shown in Table 2.

The preferred result for E1 is a ~4 km rupture with an azimuth 205° (clockwise from North), and dipping downward –26° from horizontal. For E2 two possible ruptures can be starting at the

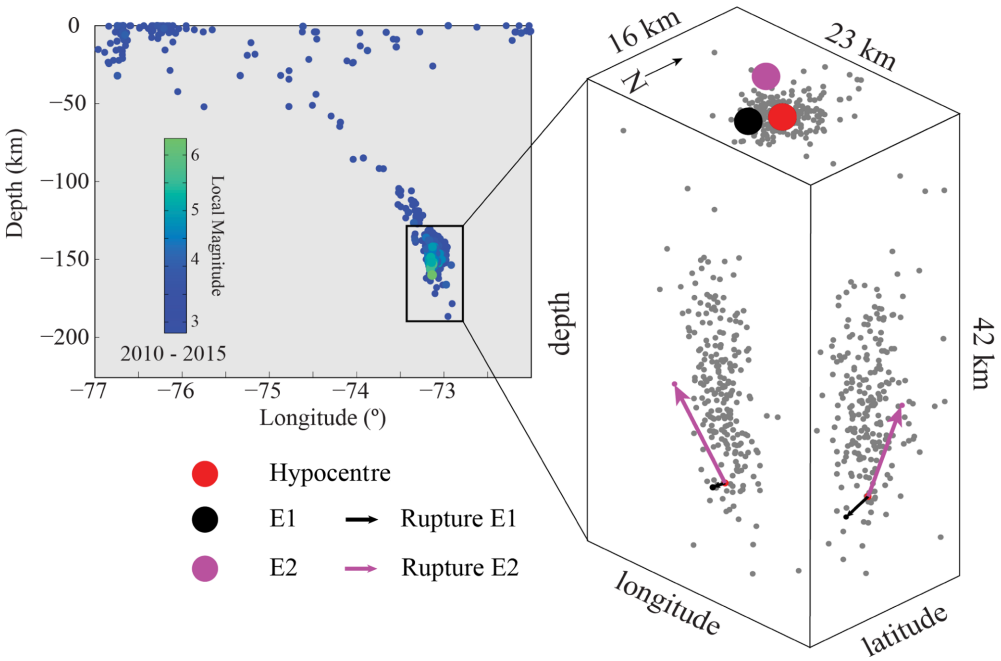

Figure 2. Subevent relative location and rupture directivity. Left-hand panel shows cross-section of the seismicity in the BN between 2010 and 2015. Right-hand panel shows the locations of the hypocentre and E1, E2 centroids with arrows indicating the rupture direction. The background seismicity shows M3+ earthquakes (grey dots) 3 months before and 1 month after the M_w 6.3 earthquake.

Table 2. Rupture parameters for subevents E1 and E2 of the M_w 6.3 Bucaramanga Nest earthquake. Centroid locations and times are obtained by double-difference relocation and are relative to the hypocentre. The horizontal (H) and vertical (L) dimensions and the rupture velocity (V_R) are estimated from the unilateral rupture. Scalar seismic moment (M_0) and radiated seismic energy (E_S) for each subevent are estimated from the STFs. Stress drop ($\Delta\sigma$) and radiation efficiency (η) are computed from the previous parameters.

Event	Centroid time (s)	Horizontal distance from hypocentre (km)	Vertical distance from hypocentre (km)	H (km)	L (km)	V_R (km s^{-1})	$M_0 \times 10^{18}$ (Nm)	$E_S \times 10^{12}$ (J)	$\Delta\sigma$ (MPa)	η
E1	1.55	3.7	+1.5	3.4	1.4	2.45	1.0684	7.80	19	0.05
E2	3.39	7.0	–6.7	7.0	–6.6	4.5	1.6026	5.20	3.3	0.2

centroid time of E1: (1) E2 starting at the centroid position of E1 and rupturing for ∼9 km towards 300°, (2) A bilateral rupture with E2 starting at the hypocentre and rupturing for 8.2 km towards 300°. Given the delay time E1–E2 being 1.8 s we obtained $Vr \sim 5.2$ km s^{-1} for case 1 and $Vr \sim 4.5$ km s^{-1} for case 2. We can further constrain the rupture geometry if we consider a 3-D unilateral rupture (Warren 2014; Zhan *et al.* 2014a) and analyse the azimuthal delay of the centroids. Comparing the relative locations and the delay of the centroids, our results suggest that the more moderate rupture velocity of 4.5 km s^{-1} is more likely for E2.

Using the parameters in Table 2 and assuming the event 2 starting at ∼1.5 s of the rupture time we calculated synthetic waveforms for comparison with actual data. The agreements between predicted and observed STFs well explain the orthogonal rupture directions between E1 and E2. The agreement is showed in Fig. 3 where observed and predicted STFs at regional and teleseismic distances are plotted.

The non-negligible CLVD component of the MT solution can be explained by allowing rotation of the focal mechanism between E1 and E2, as observed from amplitude ratios (Frohlich 1994; Fig. S6). The change in rupture direction and focal mechanism is in agreement with the wide range of focal mechanisms observed in the BN (Cortés & Angelier 2005; Prieto *et al.* 2012).

Released seismic energy and stress drop

We estimate the total energy radiated by this earthquake by integrating the average squared spectrum of the P-wave particle velocity recorded at teleseismic distances (Boatwright & Choy 1986). Prior to integrating, we must correct for the intrinsic attenuation of seismic waves caused by the Earth. The t^* parameter, describes the attenuation of seismic waves as they propagate through the Earth. To estimate a reliable t^* we first determine the apparent rupture duration τ by stacking teleseismic P wave STFs (Poli & Prieto 2014). We then grid search over a range of t^* values, and compare the observed P-wave spectra with an omega-squared model using the corner frequency $f_c \sim 1/\tau$ estimated from the source time function and the moment tensor from the CMT catalogue. Our preferred t^* (0.3 s) is the one that minimizes the misfit between the average observed and theoretical spectra for all stations. Our preferred t^* value agree with previous observation for deep earthquakes (Ye *et al.* 2013). The P wave spectra have all been corrected for geometrical spreading, the radiation pattern and attenuation, and we averaged the integrated energy flux at each station to obtain the seismic radiated energy (Boatwright & Choy 1986). The average spectrum from the global P-wave data is shown in Fig. S7. To account for the finite bandwidth (the highest observed frequency is 2 Hz), we

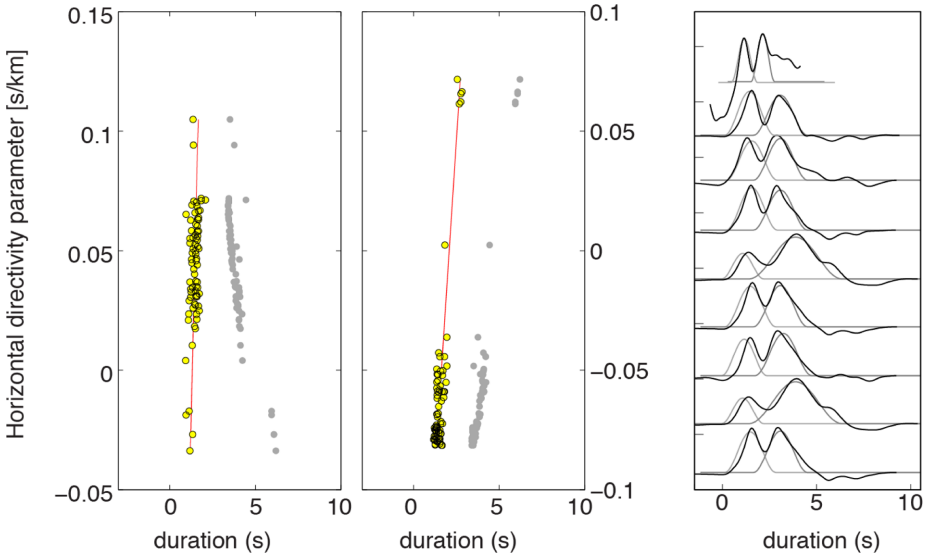

Figure 3. Left-hand panels: observed centroid times for E1 and E2 (grey) and corrected centroid times along the horizontal directivity parameter (yellow dots). Difference between observed and corrected times suggests that a significant vertical rupture is present. Right-hand panel: selected apparent STFs from teleseismic and regional stations (black) and predicted STF for E1 and E2 (grey). Our bidirectional model provides good agreement of centroid times and widths of E1 and E2 even though the durations are not used in the determination of the rupture velocities.

extrapolated the spectrum to 200 Hz, assuming an omega-squared decay.

The estimated total radiated energy of the M_w 6.3 BN earthquake is 1.3×10^{13} Joules. The scaled energy ($e = \mathrm{Er/Mo}$) is $\sim 3 \times 10^{-6}$, fundamentally lower than the typical values observed for crustal earthquakes (Ide & Beroza 2001). We use our fitted STFs corrected for radiation pattern and rupture propagation to determine the relative radiated energy of each event (Fig. 4a). While mapping the radiated energy back to the source is complex (Rivera & Kanamori 2005), we here assume that energy is radiated near the corner frequency (e.g. Kaneko & Shearer 2015) and we only aim to track the time dependence of energy release to discuss the different part of the rupture. Because of the limited frequency of the source time function, it is not possible to directly estimate the energy released, we thus set the energy at the end of the source time function being equal to the radiated energy estimated from spectral analysis (Fig. S7). We further test the difference in time energy release by analysing the single station STFs in different frequency band, showing how the first part of the rupture contains less high frequency energy (Fig. S8). Following our analysis we estimated E1 and E2 to contribute 60 and 40 per cent of the total radiated energy, respectively.

We calculated the stress drop assuming the rupture being composed of two circular cracks. For each one we calculated the radius from the measured duration of the subevent (Boatwright 1980) and using the relative moment (Table 2) and the obtained rupture velocities we obtained the stress drop (Eshelby 1957). From the estimates of radiated energies and the static source parameters (Table 2) we determine radiation efficiency $\eta = 2\mu E_S/(M_0 \Delta\sigma)$ of 0.05 and 0.2 for E1 and E2, respectively. Recent estimates of radiation efficiencies of moderate BN events (Prieto *et al.* 2013) show a very dissipative mechanism similar to E1, with a potential for thermal shear runaway. Furthermore, in contrast to the observed moment rate function, the cumulative radiated energy (Figs 4a and S7) shows very little radiation during the first second of rupture. Then after about one second from the origin time, significant seismic radiation is observed and E2 is triggered.

DISCUSSION AND CONCLUSIONS

The M_w 6.3 BN earthquake rupture process can be divided into two stages (Fig. 4b). A slow rupture characterizes stage 1, with low efficiency suggesting a high frictional stress. The low rupture velocity and high stress drop is similar to smaller dissipative events in the Bucaramanga area (Prieto *et al.* 2013). A significant portion of the available potential energy goes into breakdown work (Cocco *et al.* 2006) potentially heating the fault zone and leading to melting and extreme weakening that leads to the next stage. In stage 2, a new rupture develops towards the W–NW (E2), which radiates energy more efficiently at fast rupture velocities. This last stage could be a interpreted as a second weakening process as proposed by Kanamori & Heaton (2000), where the frictional stress dramatically drops to low values after a certain critical slip distance is reached when melting and/or other thermally driven weakening mechanism reduces friction. Laboratory and geological observations of large frictional strength reduction also show such extreme weakening, although the interpreted mechanisms may vary (Fialko & Khazan 2005; Di Toro *et al.* 2006, 2011; Green II *et al.* 2015). A possible alternative scenario is given by the triggering of the second event by the strong weakening process in place during the first event (Meng *et al.* 2012).

Seismically determined source parameters (magnitude, stress drop, radiated energy) outline the energy release during earthquake rupture and provide key constraints on the weakening mechanisms that have been observed in earthquake analog experiments (Fialko & Khazan 2005; Di Toro *et al.* 2006; Kaleman & Hirth 2007; Green II *et al.* 2015). The inferred dynamic behaviour of the earthquake suggests a cascading triggering mechanism (Chen *et al.* 2014) driven by thermal shear runaway (John *et al.* 2009; Chang *et al.* 2012), with large and fast rupture propagation being possible after a first weakening process during which most of the energy goes into heating the fault region, and the frictional stress remain high. The latter conditions allow for the runaway process to drastically reduce the dynamic frictional stress (Di Toro *et al.* 2006, 2011; Green II *et al.* 2015) and viscous effects (Fialko & Khazan 2005).

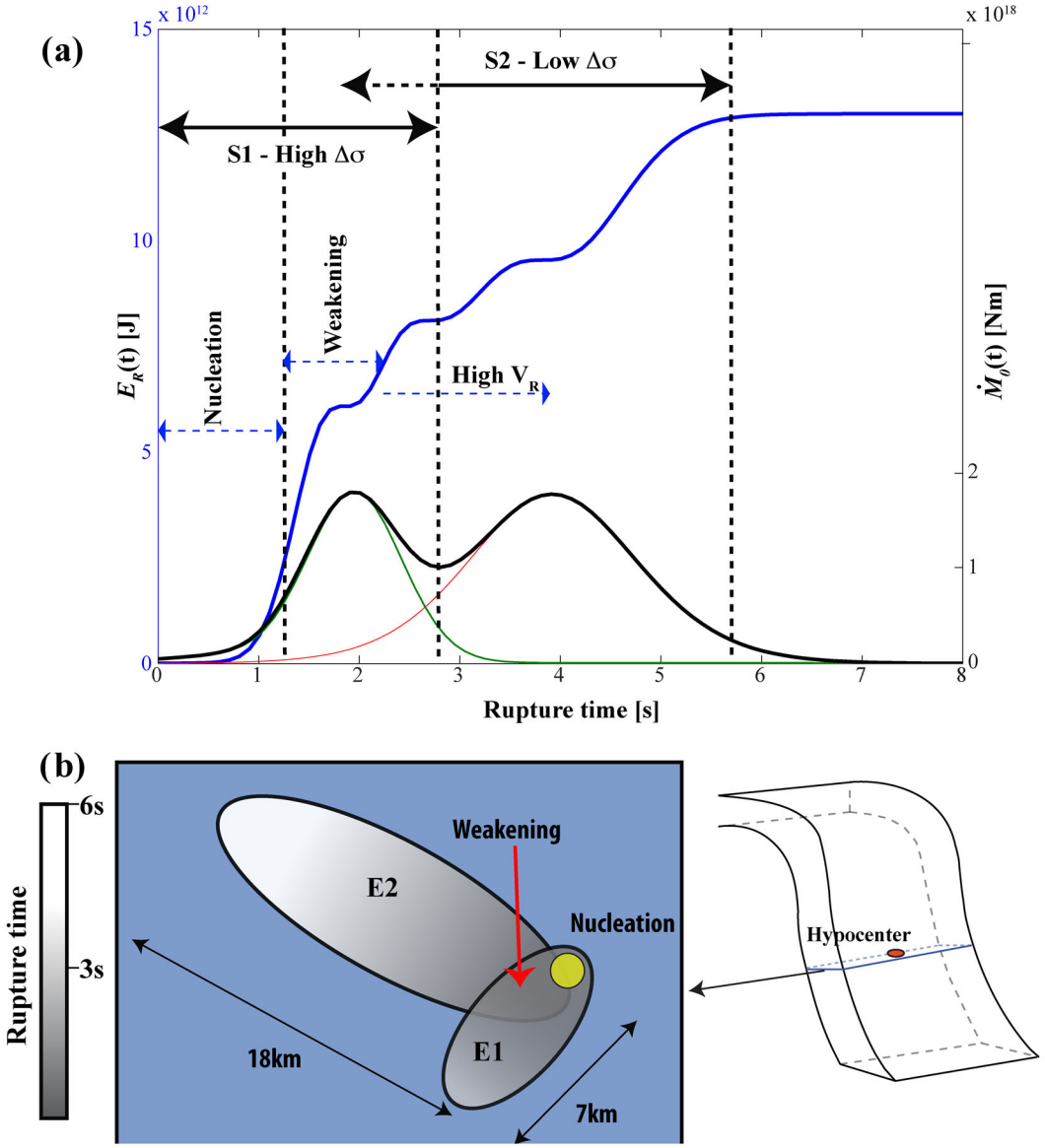

Figure 4. Model of the M_w 6.3 Bucaramanga nest rupture process. (a) Cumulative radiated energy (blue) as a function of rupture time, estimated from the observed source time function (black). Estimated source time functions for subevents E1 (green) and E2 (red) are also shown. The black dashed lines separate the three stages of the rupture process. (b) Schematic model of the rupture process projected onto a horizontal plane on the subducted plate (see inset) showing the spatial and temporal features of E1 and E2. Yellow dot represents the hypocentre.

Thru our analysis a tentatively estimation of D_c is possible. Being the average slip at the end of E1 ~0.6 m and given the beginning of high energy radiation observed for the second event at the end of event 1, we estimated the weakening distance to be of the order of the same order. This observation is supported by previous observation (Prieto *et al.* 2013) and agrees with the low efficiency observed for event 1 [e.g. $D_c = (1–\eta)\ D = 0.57$ m, with D being the average slip].

Based on the timing of the initiation of E2, the efficiency of E1 and the source scaling in the Bucaramanga Nest (Prieto *et al.* 2013), the critical weakening distance (D_c) may be of the order of ~0.5 m. This value is an order of magnitude larger than those predicted based on extrapolation of laboratory experiments (Di Toro *et al.* 2011; Schubnel *et al.* 2013; Green II *et al.* 2015) suggesting that the weakening mechanism requires fracture energy accumulation. The nature of the weakening mechanism is an active area of research, and our seismological observations highlight the importance of thermally controlled processes in both intermediate-depth and deep earthquake rupture. Whether the mechanism is purely thermal or related to phase and dehydration reactions requires a combination of observational, laboratory and theoretical studies that we hope to pursue.

ACKNOWLEDGEMENTS

The authors would like to thank two reviewers and the associate editor for helpful suggestions that helped improve the paper. This work was supported by NSF grant EAR-1521534. H.A. acknowledges São Paulo Research Foundation (FAPESP) grant #2014/26330-0. Support for field and research in Colombia was in part provided by Colciencias, agreement.

REFERENCES

Bianchi, M. *et al.*, 2014. The New Brazilian Seismic Network: current status and detectability test with the recent Pisagua Earthquake Sequence, Northern Chile, *Earth Sci. Res. J.,* **18**(Special Issue July), 262–263.

Boatwright, J., 1980. A spectral theory for circular seismic sources; simple estimates of source dimension, dynamic stress drop, and radiated seismic energy, *Bull. seism. Soc. Am.,* **70**(1), 1–27.

Boatwright, J. & Choy, G.L., 1986. Teleseismic estimates of the energy radiated by shallow earthquakes, *J. geophys. Res: Solid Earth (1978–2012),* **91**(B2), 2095–2112.

Chang, J.C., Lockner, D.A. & Reches, Z., 2012. Rapid acceleration leads to rapid weakening in earthquake-like laboratory experiments, *Science,* **338,** 101–105.

Chen, Y., Wen, L. & Ji C., 2014. A cascading failure during the 24 May 2013 great Okhotsk deep earthquake, *J. geophys. Res.: Solid Earth,* **119**(4), 3035–3049.

Cocco, M., Spudich, P. & Tinti, E., 2006. On the mechanical work absorbed on faults during earthquake ruptures, in *Earthquakes: Radiated Energy and the Physics of Faulting,* pp. 237–254, American Geophysical Union.

Cortés, M. & Angelier, J., 2005. Current states of stress in the northern Andes as indicated by focal mechanisms of earthquakes, *Tectonophysics,* **403**(1), 29–58.

Di Toro, G., Hirose, T., Nielsen, S., Pennacchioni, G. & Shimamoto, T., 2006. Natural and experimental evidence of melt lubrication of faults during earthquakes, *Science,* **311,** 647–649.

Di Toro, G. *et al.*, 2011. Fault lubrication during earthquakes, *Nature,* **471,** 494–498.

Eshelby, J., 1957. The determination of the elastic field of an ellipsoidal inclusion, and related problems, *Proc. R. Soc. Lond., A: Math. Phys. Eng. Sci.,* **241**(1226), doi:10.1098/rspa.1957.0133.

Fialko, Y. & Khazan, Y., 2005. Fusion by earthquake fault friction: stick or slip?, *J. geophys. Res.: Solid Earth (1978–2012),* **110**(B12), doi:10.1029/2005jb003869.

Frohlich, C., 1994. Earthquakes with non—double-couple mechanisms, *Science,* **264**(5160), 804–809.

Frohlich, C., 2006. *Deep Earthquakes,* Cambridge Univ. Press.

Green, H.W. & Houston, H., 1995. The mechanics of deep earthquakes, *Annu. Rev. Earth planet. Sci.,* **23,** 169–214.

Green II, H.W., Shi, F., Bozhilov, K., Xia, G. & Reches, Z., 2015. Phase transformation and nanometric flow cause extreme weakening during fault slip, *Nat. Geosci.,* **8,** 484–489.

Houston, H., 2007. Deep earthquakes, in *Treatise on Geophysics*, Vol. 4: Deep Earthquakes, pp. 321–350, ed. Schubert, G., Elsevier.

Ide, S. & Beroza, G.C., 2001. Does apparent stress vary with earthquake size?, *Geophys. Res. Lett.,* **28**(17), 3349–3352.

Kelemen, P.B. & Hirth, G., 2007. A periodic shear-heating mechanism for intermediate-depth earthquakes in the mantle, *Nature,* **446**(7137), 787–790.

Kanamori, H. & Heaton, T.H., 2000. Microscopic and macroscopic physics of earthquakes, *Geocomplexity and the Physics of Earthquakes,* pp. 147–163, eds Rundle, J.B., Turcotte, D.L. & Klein, W., American Geophysical Union.

Kanamori, H., Anderson, D.L. & Heaton, T.H., 1998. Frictional melting during the rupture of the 1994 Bolivian earthquake, *Science,* **279**(5352), 839–842.

Kaneko, Y. & Shearer, P.M., 2015. Variability of seismic source spectra, estimated stress drop, and radiated energy, derived from cohesive-zone models of symmetrical and asymmetrical circular and elliptical ruptures, *J. geophys. Res.: Solid Earth,* **120**(2), 1053–1079.

John, T., Medvedev, S., Rüpke, L.H., Andersen, T.B., Podladchikov, Y.Y. & Austrheim, H., 2009. Generation of intermediate-depth earthquakes by self-localizing thermal runaway, *Nat. Geosci.,* **2,** 137–140.

Meng, L., Ampuero, J.P., Stock, J., Duputel, Z., Luo, Y. & Tsai, V.C., 2012. Earthquake in a maze: compressional rupture branching during the 2012 Mw 8.6 Sumatra earthquake, *Science,* **337**(6095), 724–726.

Ojeda, A. & Havskov, J., 2001. Crustal structure and local seismicity in Colombia, *J. Seismol.,* **5**(4), 575–593.

Poli, P. & Prieto, G., 2014. Global and along-strike variations of source duration and scaling for intermediate-depth and deep-focus earthquakes, *Geophys. Res. Lett.,* **41**(23), 8315–8324.

Prieto, G.A., Parker, R.L. & Vernon III, F.L., 2009. A Fortran 90 library for multitaper spectrum analysis, *Comput. Geosci.,* **35**(8), 1701–1710.

Prieto, G.A., Beroza, G.C., Barrett, S.A., López, G.A. & Florez, M., 2012. Earthquake nests as natural laboratories for the study of intermediate-depth earthquake mechanics, *Tectonophysics,* **570,** 42–56.

Prieto, G.A., Florez, M., Barrett, S.A., Beroza, G.C., Pedraza, P., Blanco, J.F. & Poveda, E., 2013. Seismic evidence for thermal runaway during intermediate-depth earthquake rupture, *Geophys. Res. Lett.,* **40**(23), 6064–6068.

Richardson, E. & Jordan, T.H., 2002. Low-frequency properties of intermediate-focus earthquakes, *Bull. seism. Soc. Am.,* **92**(6), 2434–2448.

Rivera, L. & Kanamori, H., 2005. Representations of the radiated energy in earthquakes, *Geophys. J. Int.,* **162**(1), 148–155.

Rondenay, S., Bostock, M.G. & Fischer, K.M., 2005. Multichannel inversion of scattered teleseismic body waves: practical considerations and applicability, in *Seismic Earth: Array Analysis of Broadband Seismograms,* pp. 187–203, eds Levander, A. & Nolet, G., American Geophysical Union.

Schubnel, A., Brunet, F., Hilairet, N., Gasc, J., Wang, Y. & Green, H.W., 2013. Deep-focus earthquake analogs recorded at high pressure and temperature in the laboratory, *Science,* **341**(6152), 1377–1380.

Seber, G.A.F. & Wild, C.J., 2003. *Nonlinear Regression,* Wiley-Interscience.

Sokos, E.N. & Zahradnik, J., 2008. ISOLA a Fortran code and a Matlab GUI to perform multiple-point source inversion of seismic data, *Comput. Geosci.,* **34**(8), 967–977.

Vallée, M., Charléty, J., Ferreira, A.M.G., Delouis, B. & Vergoz, J., 2011. SCARDEC: a new technique for the rapid determination of seismic moment magnitude, focal mechanism and source time functions for large earthquakes using body wave deconvolution, *Geophys. J. Int.,* **184,** 338–358.

VanDecar, J.C. & Crosson, R.S., 1990. Determination of teleseismic relative phase arrival times using multi-channel cross-correlation and least squares, *Bull. seism. Soc. Am.,* **80**(1), 150–169.

Warren, L.M., 2014. Dominant fault plane orientations of intermediate-depth earthquakes beneath South America, *J. geophys. Res.: Solid Earth,* **119**(7), 5762–5785.

Waldhauser, F. & Ellsworth, W.L., 2000. A double-difference earthquake location algorithm: method and application to the northern Hayward fault, California, *Bull. seism. Soc. Am.,* **90**(6), 1353–1368.

Wiens, D.A., 2001. Seismological constraints on the mechanism of deep earthquakes: temperature dependence of deep earthquake source properties, *Phys. Earth planet. Inter.,* **127**(1), 145–163.

Wiens, D.A. & Gilbert, H.J., 1996. Effect of slab temperature on deep-earthquake aftershock productivity and magnitude-frequency relations, *Nature,* **384**(6605), 153–156.

Ye, L., Lay, T., Kanamori, H. & Koper, K.D., 2013. Energy release of the 2013 Mw 8.3 Sea of Okhotsk earthquake and deep slab stress heterogeneity, *Science,* **341**(6152), 1380–1384.

Yu, W.C. & van der Hilst, R.D., 2013. Removing source-side scattering for virtual deep seismic sounding (VDSS), *Geophys. J. Int.,* **195**(3), 1932–1941.

Zhan, Z., Helmberger, D.V., Kanamori, H. & Shearer, P.M. 2014a. Supershear rupture in a Mw 6.7 aftershock of the 2013 Sea of Okhotsk earthquake, *Science,* **345**(6193), 204–207.

Zhan, Z., Kanamori, H., Tsai, V.C., Helmberger, D.V. & Wei, S., 2014b. Rupture complexity of the 1994 Bolivia and 2013 Sea of Okhotsk deep earthquakes, *Earth planet. Sci. Lett.,* **385,** 89–96.

SUPPORTING INFORMATION

Additional Supporting Information may be found in the online version of this paper:

Figure S1. Regional moment tensor solution of the M_w 6.3 Bucaramanga Nest Earthquake. (a) Map of regional stations and M_w 6.2 hypocentre. (b) Cross section of the M_w 6.3 event (red) and aftershocks (black) along the line in (a). (c) Estimated focal mechanism and (d) The correlation coefficient as a function of source depth (5 km interval) for inverted regional moment tensors and the corresponding DC per cent for each solution.

Figure S2. Broad-band waveform comparison between observed (red) and synthetic (black) data. Synthetics are computed using the moment tensor solution given in (b). Numbers indicate peak displacement (in metres) of observed data. Grey traces were not used in the MT inversion.

Figure S3. Observations of apparent source time functions (coloured lines) at various teleseismic subarrays using MCCC and PCA. Dashed coloured lines below STFs are the predictions based on our rupture model. Two subevents E1 and E2 are clearly observed at all stations along with azimuthal variation in STF duration and relative amplitudes of E1 and E2. The focal sphere shows the MT solution planes and first motion polarities for all stations (positive '+' and negative 'o').

Figure S4. SH-Polarities and selected STFs for the M_w 6.3 Bucaramanga Nest earthquake. Note the clear polarity change in the northern quadrant, which is in agreement with the proposed focal mechanism. Positive polarity STF are shown in red, negative polarity in black, and undetermined in grey.

Figure S5. Observed and predicted arrival time differences between the hypocentre *P*-wave arrival times and E1 (a) and E2 (b) centroids ad between the E2–E2 centroids (c). These time differences are used to determine the relative locations shown in Fig. 2. Note that the relative times of E2 w.r.t. the hypocentre and E1 are similar, suggesting that E2 is shallower compared to both.

Figure S6. Estimated amplitudes of each subevent and amplitude ratios from regional and teleseismic *P* waves. The amplitude ratio for two events with the same focal mechanism is expected to be constant, while here it shows that the focal mechanism of the 2 events is slightly rotated. Estimated rotation of the focal mechanism of E2 (red lines) assuming E1 has same focal mechanism as the broad-band moment tensor solution (beach-ball). Yellow lines shows range of viable mechanisms for E2.

Figure S7. Global average spectrum of *P* waves (blue) and omega-squared model (red dashed line). The total radiated energy from this earthquake is 1.3e13J (see supplementary text).

Figure S8. Energy radiation for an apparent source time function at azimuth 330° and distance 40°. The source time function (red trace) is corrected for the T^* value obtained from spectral analysis. We then filter the source time function in a long period (0.05–0.5 Hz) an short period (0.5–2 Hz) frequency bands, and the integral of the squared velocity waveform is calculated. As evident the first part of the rupture is dominated by long period radiation (blue trace). The second and more efficient part of the rupture radiates larger high frequency energy (green trace). The crossover between the two energy accumulation functions occurs at time ∼1.5 s, the time interpreted as the moment at which the extreme weakening process is occurring (see main text) (http://gji.oxfordjournals.org/lookup/suppl/doi:10.1093/gji/ggw065/-/DC1).

Please note: Oxford University Press is not responsible for the content or functionality of any supporting materials supplied by the authors. Any queries (other than missing material) should be directed to the corresponding author for the paper.